

We are IntechOpen, the world's leading publisher of Open Access books Built by scientists, for scientists

6,900

Open access books available

186,000

International authors and editors

200M

Downloads

Our authors are among the

154

Countries delivered to

TOP 1%

most cited scientists

12.2%

Contributors from top 500 universities



WEB OF SCIENCE™

Selection of our books indexed in the Book Citation Index
in Web of Science™ Core Collection (BKCI)

Interested in publishing with us?
Contact book.department@intechopen.com

Numbers displayed above are based on latest data collected.
For more information visit www.intechopen.com



Organic-Inorganic Hybrid Coatings for Active and Passive Corrosion Protection

Andressa Trentin, Samarah V. Harb, Thiago A.C. de Souza, Mayara C. Uvida and Peter Hammer

Abstract

Organic-inorganic coatings based on poly(methyl methacrylate) (PMMA)-silica and PMMA-cerium oxide hybrids provide effective and active corrosion protection of metallic surfaces. For both hybrid materials, the covalent conjugation of inorganic silica or ceria nanodomains with the PMMA matrix, provided by molecular coupling agents, leads to homogenous and highly cross-linked nanocomposites, which act in the form of coatings as an efficient diffusion barrier. The addition of lithium salts (500–2000 ppm) into PMMA-silica hybrid and optimized ceria fraction in PMMA-cerium oxide coatings results in active corrosion inhibition by the self-healing effect. Results of electrochemical assays of aluminum- and steel-coated samples, performed in a 3.5% NaCl solution, show an excellent corrosion resistance (impedance modulus up to $100 \text{ G}\Omega \text{ cm}^2$) and durability (up to 350 days) of the 10- μm -thick passive barrier layer. Time-of-flight secondary ion mass and X-ray photoelectron spectroscopies evidenced the self-healing ability of coatings induced by lithium/cerium ion leaching toward corrosion spots or artificial scratches, which are restored by a protective layer of precipitated phases. Results presented in this book chapter evidence the active role of lithium and cerium species in improving the hybrid structure and providing through self-healing a significantly extended service life of metallic components.

Keywords: anticorrosion coating, organic-inorganic hybrid, passive and active protection, corrosion inhibitors, self-healing, AA7075, carbon steel

1. Introduction

The development of efficient production techniques of metallic alloys in the late twentieth century formed the basis for the boom of construction, transportation, energy, packaging, and electronic industries [1, 2]. Although extensively used, unprotected alloys are subject to a constant oxidation process, either in contact with humid atmosphere, aqueous, or soil systems, turning them into natural ore [1, 3]. One common approach to prevent or at least delay metallic corrosion is the application of organic coatings as a physical diffusion barrier. A barrier coating in the form of a dense insulating layer acts as a quasi-ideal capacitor, which

inhibits the contact of corrosive species, such as the electrolyte, with the substrate. Barrier coatings based on acrylate, epoxy, and polyurethane are extensively employed in automotive, aviation, and marine industries but also in electronics, decoration, food, and beverage items. However, if these coating systems are not designed to withstand aggressive environments, they fail, causing corrosion of the underlying alloy. Therefore, conventional high-efficiency coatings are prepared in the form of multilayers combining a chromate conversion layer (0.1–0.2 μm) with a primer (commonly an epoxy layer of about 15–25 μm loaded with corrosion inhibitors) and an organic topcoat, mostly in the form of a 50–100- μm -thick polyurethane, which provide barrier, decorative, hydrophobic, and UV-resistant characteristics [4, 5].

Chromates, widely employed as conversion layer in the aerospace industry, provide effective protection because the excess of non-reduced ions produces an extremely corrosion-resistant film composed of mixed Cr and Al oxides [6]. However, hexavalent chromium causes occupational health problems due to carcinogenic and mutagenic effects [7], which led to an intense search for high-performance chromium-free coatings able to protect passively and actively metal surfaces in harsh environments. To achieve this goal, the alternative material must provide (i) a dense passive barrier with a very low permeation rate and after failure (ii) actively inhibit corrosive processes with similar efficiency as the self-healing ability of chromate anions. Considering this challenge, considerable efforts have been spent by the scientific community to develop alternatives to chromium conversion coatings, and some encouraging results have been already achieved.

One promising class of coating systems, developed in the last decade, which fulfill the cited criteria, is organic-inorganic nanocomposites based on conventional acrylic, epoxy, and polyurethane materials combined with ceramic nanofillers, such as silica, ceria, zirconia, etc. These hybrid materials have demonstrated excellent barrier property, providing long-term protection for steel and aluminum alloys [3, 8–10]. The superiority of hybrid systems compared to purely polymeric phases comes from a tailored nanostructure achieved by proper amounts of inorganic nanofillers within the organic matrix and the careful tuning of synthesis conditions, resulting in a dense and homogeneous nanocomposite that acts as an efficient diffusion barrier, limiting the water uptake and diffusion of ionic species to a very low rate [11]. The inorganic nodes have the important role to densify the structure by anchoring covalently the polymeric chain segments through a cross-linking agent and to improve the adhesion at the coating/metal interface through covalent bonding [12–14]. The function of the polymeric phase is to provide minimum internal stress and porosity of the hybrid network, hermetically sealing the structure [3, 11, 12]. Hence, the key factor for the stability of the material under adverse conditions is the covalent conjugation between the two phases through the coupling molecule that has functional similarity to both parts. The presence of this organic-inorganic interphase overcomes the limitations of organic systems such as lack of thermal and mechanical stability, poor adhesion, and presence of voids due to material swelling [15–18].

Nevertheless, even the best barrier fails after some time due to the permeation of water and aggressive species under weathering or mechanical damage. Smart coatings are an emerging technology to bypass the limitations of passive systems, providing a repair response mechanism after failure [5]. Several approaches have been developed in the search for chromium-free organic coatings using organic and inorganic additives for extrinsic self-healing strategies. These types of coatings are able to respond after local damage through reactions triggered by variations in pH, temperature, presence of water, mechanical damage, and UV [3, 4, 19].

In practice, however, some studied coating systems, especially those based on inhibitor-filled micro- and nano-containers, imply increasing costs, which are hardly accepted by the industry. Some recent studies reporting on incorporation of simple additives, such as PANI [20], TiO₂ [21], ZnO [22], lithium [23, 24], ZrO₂ [9, 25], cerium/ceria [26–29], poly(2-butylaniline) (P2BA) [30], polydopamine (PDA) [31], 2-mercaptobenzimidazole (MBI) [32], and tannins [33], among others, have shown promising results toward the development of chromium-free active coatings. This chapter comprises an overview of efficient passive organic-inorganic coatings and their modified form for active protection of metal surfaces. Emphasis is given on inorganic additives that meet the current demand for non-toxic low-cost substances, such as cerium nanoparticles and lithium ions in hybrid matrices.

2. Organic-inorganic hybrid coatings

2.1 Passive protection

Organic-inorganic coatings are usually prepared by combining the polymerization of the organic phase using an anionic, cationic, thermal, or photo initiator with the sol-gel route of hydrolysis and condensation of an inorganic compound in the form of silicon, zirconium, aluminum, and titanium alkoxides [34]. In the next step, the hybrid sol is applied on the metal surface by spray, spin, or dip coating methods, and then the obtained film is dried and cured prior to the structural, thermal, mechanical, and electrochemical analysis.

Epoxy [35–38] and polyurethanes-based [21, 39, 40] hybrid coatings present excellent protection against metallic corrosion; however recent research has shown that equal or even better results in terms of corrosion resistance and durability can be achieved with much thinner layers, based on acrylic or epoxy hybrids. Especially for poly(methyl methacrylate) (PMMA)-silica coatings, remarkable results have been reported when applied on carbon steel and aluminum alloys. For instance, using electrochemical impedance spectroscopy (EIS) assays, Hammer et al. reported that PMMA-silica coatings with thicknesses between 1.5 and 3 μm are able to withstand adverse conditions without failure for 18 days immersed in 3.5% NaCl, while maintaining the low-frequency impedance modulus ($|Z_{if}|$) in the GΩ cm² range, a value about five orders of magnitude higher than that of bare steel [41]. Analyzing the structural properties of this material, dos Santos et al. showed that optimizing the inorganic solvent proportion (ethanol/H₂O ratio) results in higher connectivity of the silica phase, leading to an improvement of the corrosion protection ($|Z_{if}| > 1 \text{ G}\Omega \text{ cm}^2$) and durability up to 6 months in 3.5% NaCl and more than 3 months in saline/acid solution [12].

Excellent passive corrosion protection of carbon steel was recently reported for some micrometer-thick PMMA-silica coatings in a study where the ratio of thermal initiator (benzoyl peroxide (BPO)) to monomer (methyl methacrylate (MMA)) was varied in the range of 0.01–0.1 (B001, B005, B010 samples) [11]. The authors found that this parameter strongly influences the hybrid structure in terms of polymerization efficiency, leading to an improved anticorrosion performance. From Raman spectra (**Figure 1a**), it can be observed that as the BPO fraction increased, the C=C band at 1640 cm⁻¹ disappeared, indicating that the larger number of radicals provided by BPO promotes a more efficient polymerization of MMA. This result is supported by thermogravimetry, carried out under N₂ atmosphere to analyze the decomposition stages of the hybrid structure (**Figure 1b**). The first

derivative of the thermogravimetric (TG) curves (**Figure 1c**) shows that the PMMA phase has three major degradation events, involving the rupture of head-to-head segments (stacking defects) at about 240°C (T_1), breaking of unsaturated chain ends at $\sim 300^\circ\text{C}$ (T_2), and a random breaking of head-tail segments at $\sim 400^\circ\text{C}$ (T_3). The differential thermogravimetric (DTG) curves clearly show that the stacking defects (T_1 event) are strongly suppressed for higher BPO/MMA ratios, evidencing improved polymerization. The residual mass of about 20 wt% found at 800°C corresponds to the nominal fraction of the silica phase in the hybrid.

In this study it was shown that the combination of adequate proportions between reactive groups of organic monomer (MMA), silica precursor (tetraethoxysilane (TEOS)), and coupling agent (3-(trimethoxysilyl)propyl methacrylate (MPTS)) leads to the formation of a homogeneous and defect-free structure

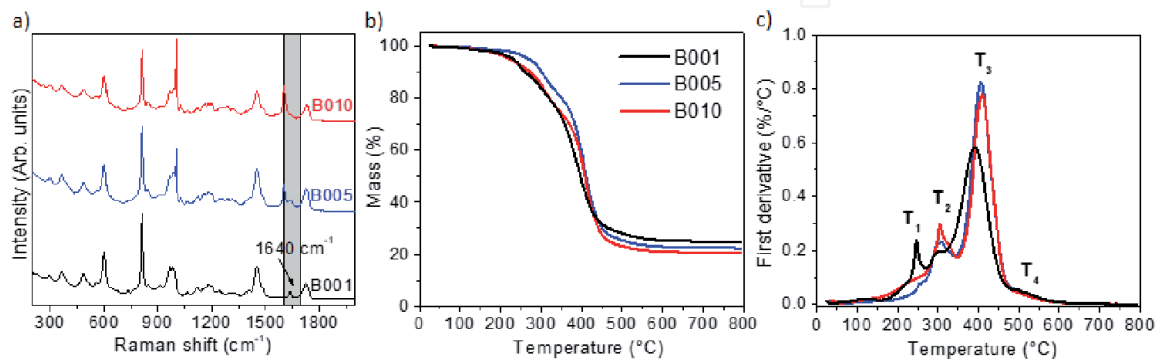


Figure 1.

(a) Raman spectra, (b) TG curves and (c) DTG curves of PMMA-silica hybrids prepared using BPO/MMA ratios of 0.01, 0.05, and 0.10 (reproduced with permission from Elsevier [11]).

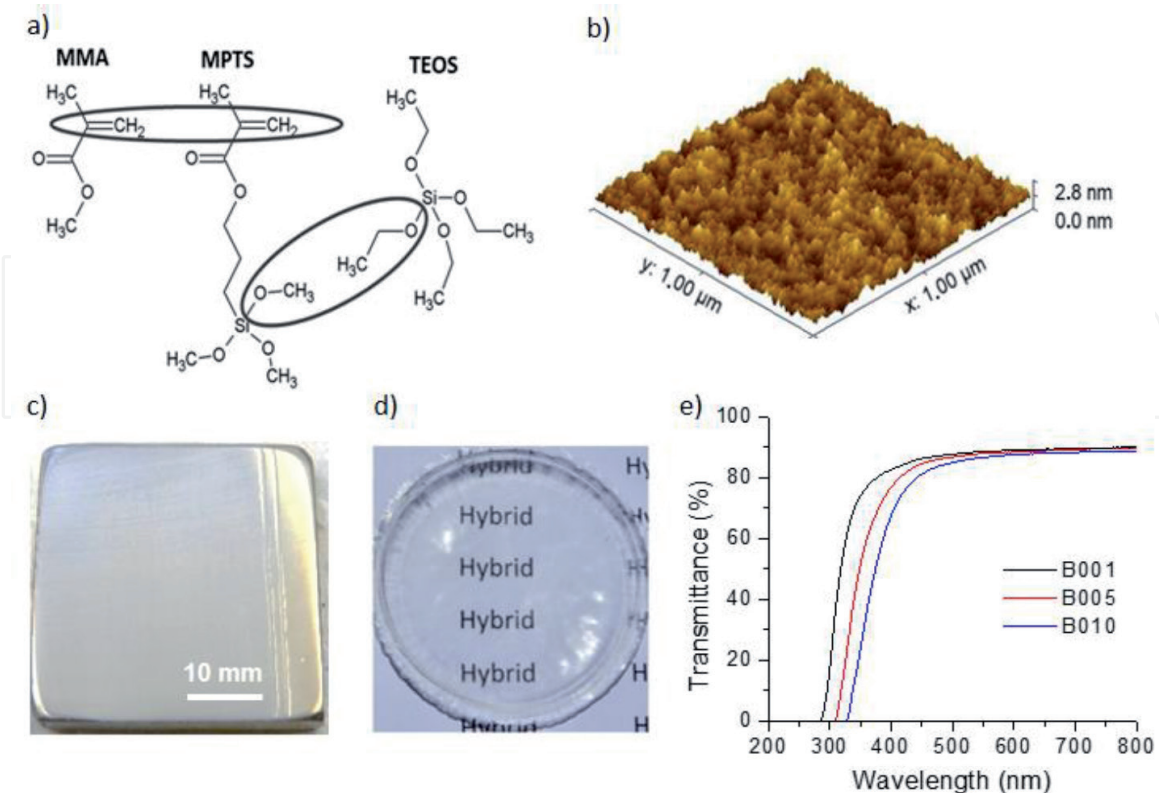


Figure 2.

(a) Representation of the molecular structure of the PMMA-silica hybrid precursors, showing the reactive groups of MMA and silicon alkoxides; (b) 3D AFM topography image of the B001 coating deposited on carbon steel; (c) representative images of the coated carbon steel; (d) unsupported hybrid; (e) UV-vis transmittance spectra of the unsupported hybrids (reproduced with permission from Elsevier [11]).

(**Figure 2a**). According to atomic force microscopy (AFM), optical, and UV-vis results (**Figure 2b–e**), the prepared coatings are transparent (80–90% transmittance) and very smooth (RMS roughness <1 nm), expected features for effective barrier coatings. For increasing amounts of the thermal initiator, the red shift of the absorption edge (**Figure 2e**) may be related to increased absorption of BPO in the UVA spectral range. Furthermore, adhesion pull-off tests evidenced a strong adherence of the coatings to the steel substrate, reaching values up to 26.3 MPa for the B001 sample, while 14.8 MPa, 8.9 MPa, and 6.7 MPa were determined for the B005, B010 and pure PMMA, respectively.

To evaluate the anticorrosion performance of coated and uncoated steel, EIS measurements were performed in duplicate after immersion of the coatings in neutral 3.5% NaCl solution at regular intervals until a significant drop in the impedance modulus was observed, representing the lifespan of the coating. After 3 h of immersion, all hybrid coatings showed a quasi-ideal capacitive behavior over almost the entire frequency range, contrasting with the poor performance of pure PMMA and bare steel (**Figure 3a**).

The comparison with pure PMMA coating shows clearly the crucial role of the silica phase in increasing corrosion resistance, after 1 day of immersion, from a low-frequency impedance modulus of 200 k Ω cm² (pure PMMA) to more than 5.0 G Ω cm² (PMMA-silica coatings). Moreover, the BPO increase led to a considerable lifespan extension for the B010 coating (9.1 μ m thick) reaching 583 days with a nearly unchanged electrochemical response (**Figure 3b**), compared to the lifetime of 40–50 days, observed for the B005 and B001 coatings (5.0 and 2.8 μ m thick, respectively), and only 1 day of the PMMA film. This anticorrosion

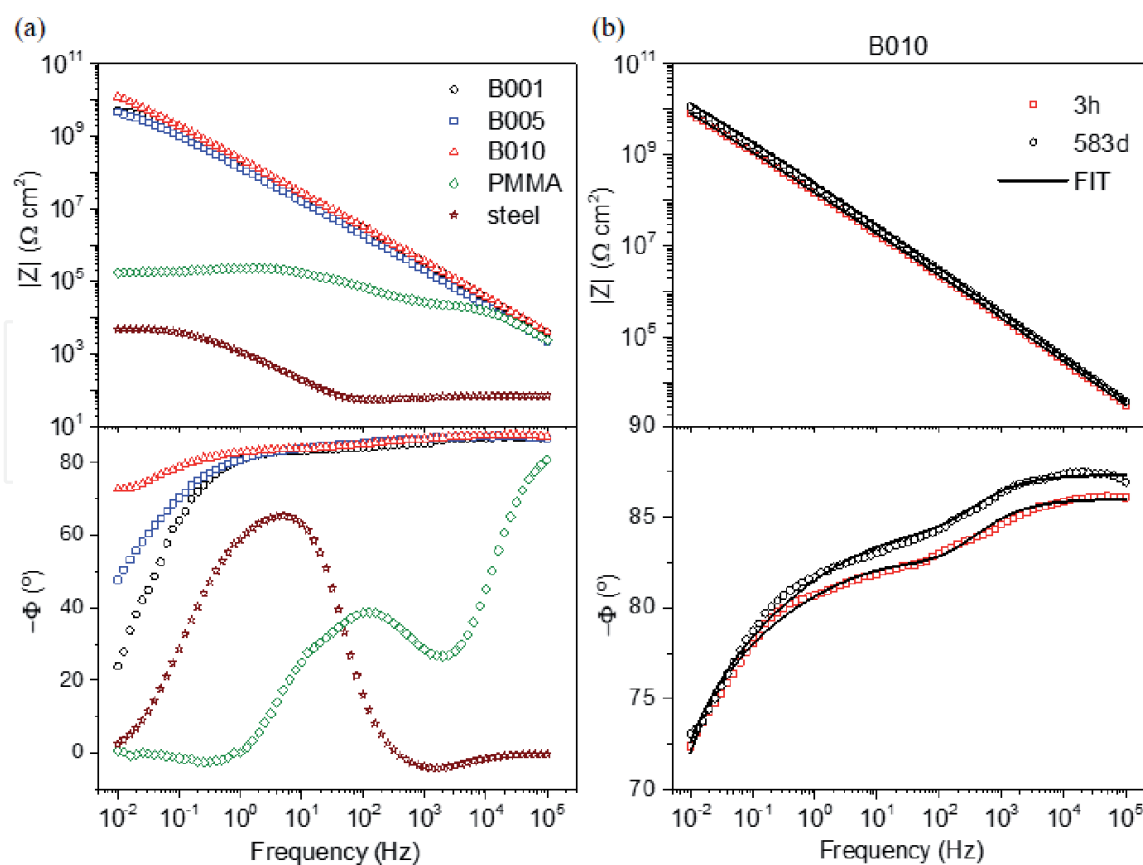


Figure 3. Bode plots recorded (a) after 3 h immersion in 3.5% NaCl, for PMMA-silica coatings on carbon steel prepared at different BPO/MMA ratios, pure PMMA (BPO/MMA = 0.01) and bare steel and (b) for different immersion times of the B010 sample. The symbols represent the experimental data, and the solid lines are fits obtained using the electrical equivalent circuit (EEC) model (reproduced with permission from Elsevier [11]).

Coating	Substrate	Thickness (μm)	$ Z_{if} $ ($\text{G}\Omega \text{cm}^2$) lifetime (days) solution	Ref.
PMMA-MPTS-TEOS	A1010 carbon steel	2.3–9.7	~5, 583, 3.5% NaCl	[11]
PMMA-MPTS-TEOS	AA2024	~3	~50, >560, 3.5% NaCl	[3]
PMMA-MPTS-TEOS	A1010 carbon steel	1.5–2	~5, 196, 3.5% NaCl	[12]
Acrylic resin-SiO ₂	Mild steel	75	~10, 90, 3.5% NaCl	[43]
PMMA-MPTS-TEOS-CNTs or GO	A1010 carbon steel	3–6	~3, 211, 3.5% NaCl	[42]
Epoxy-zinc phosphate-iron oxide	Cold rolled low carbon steel	55–140	~450/60, 220/405, 3% NaCl	[8]
Epoxy-PANI	Mild steel	20	10–100, 120, 3.5% NaCl	[20]
Epoxy-GO-P2BA	Q235 carbon steel	20	10, 80, 3.5% NaCl	[30]
PU-PANI	Mild Steel	~60	10, 58, 3.5% NaCl	[40]
PU-ZrO ₂ -SiO ₂	Carbon steel	40–55	~100, 226, 3.5% NaCl	[9]
PU-MMT	Carbon steel	~40	~10, 225, 3.5% NaCl	[39]
PU-PS-PLA-MBT	AA2024	152	~0.1, 83, 3.5% NaCl	[44]
PU-TEOS-TIP-ZRP	AA2024	203	~10, 100, 3.5% NaCl	[45]

PMMA, poly(methyl methacrylate); MPTS, 3-(trimethoxysilyl)propyl methacrylate; TEOS, tetraethoxysilane; CNTs, carbon nanotubes; GO, graphene oxide; PANI, polyaniline; MMT, montmorillonite; P2BA, poly(2-butylaniline); PU, polyurethane; PS, polysiloxane; PLA, polylactic acid; MBT, 2-mercaptobenzothiazole; TIP, titanium(IV) isopropoxide; ZRP, zirconium(IV) propoxide.

Table 1.

Reported high-performance passive hybrid coatings: composition, substrate, thickness, impedance modulus at low frequency $|Z_{if}|$, lifetime, and solution.

performance, associated with an improved structure (**Figure 1**), is comparable to that of the best performing anticorrosive coatings reported so far [8, 9, 12, 20, 21, 39, 42]. Results obtained for high-performance passive barriers based on organic-inorganic coatings reported by several research groups are summarized in **Table 1**.

Additional information on the barrier property of the B010 sample was obtained by a cross-sectional analysis using scanning electron microscopy coupled with energy dispersive X-ray analysis (SEM/EDX) before and after 583 days of immersion. **Figure 4a** shows an essentially unaffected morphology, free of pores and defects, after 583 days of immersion. Further evidence comes from the EDS profiles recorded along normal axis of the coating, shown in **Figure 4b**. The spectrum of the immersed sample shows no chlorine signal, which would indicate the presence of Cl⁻ ions in the bulk, thus confirming the excellent barrier properties of this hybrid nanocomposite.

From these results, it can be concluded that the quantity of the thermal initiator plays a crucial role in terms of the connectivity of the organic phase, resulting in a remarkable improvement of the barrier property for the B010 coating (BPO/MMA = 0.1). The increase of the impedance modulus of more than five orders of magnitude and the long durability of this coatings, compared to the pure PMMA film, highlights the crucial role of the silica phase and the importance of an efficient polymerization. Considering the excellent performance achieved by PMMA-silica coatings without any additives, this material can be considered as a promising alternative for conventional primer systems for the protection of steel surfaces.

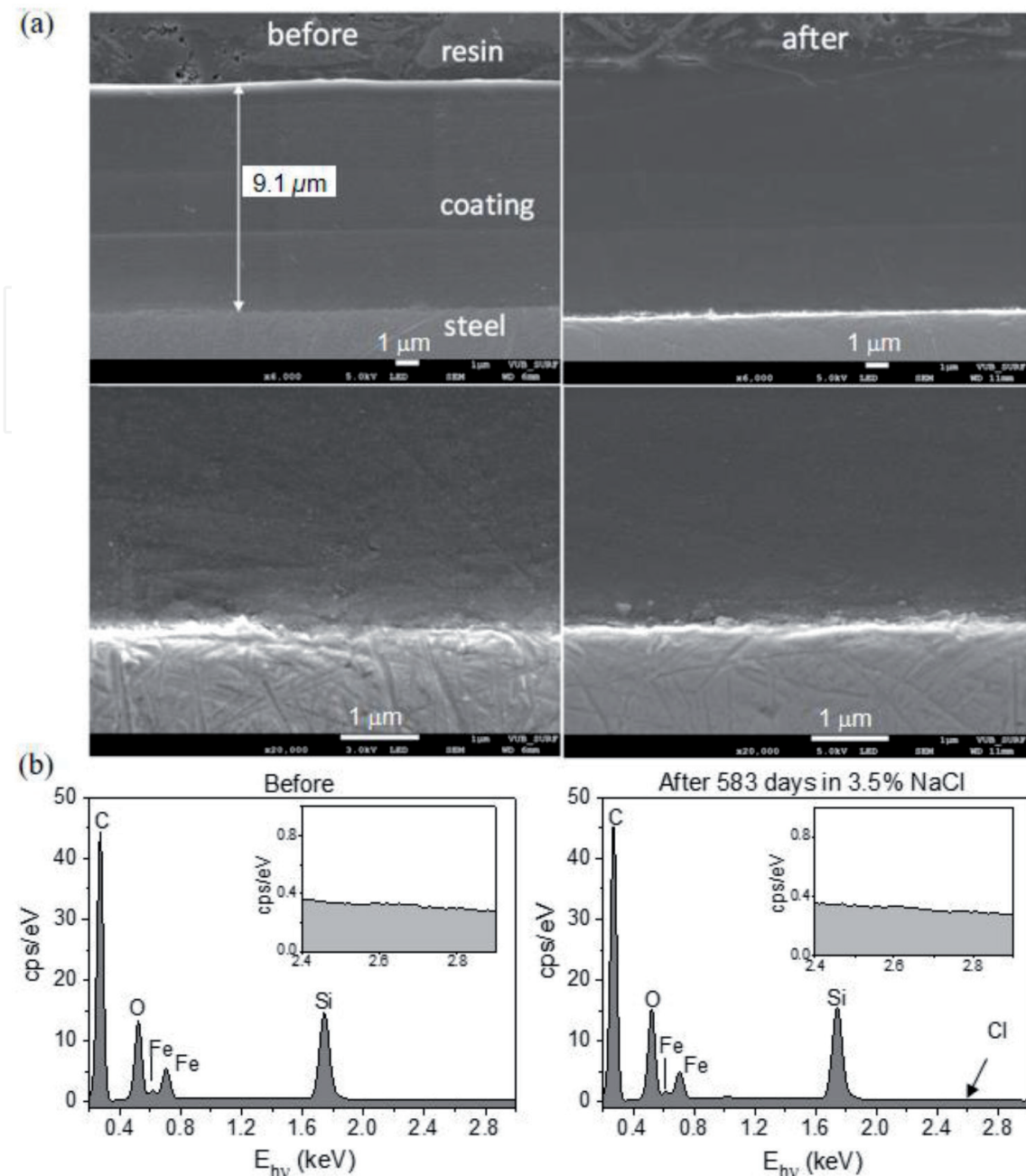


Figure 4. (a) Cross-sectional SEM images of the B010 coating, before (left) and after (right) 583 days of immersion in 3.5% NaCl solution, including details of the coating/steel interface. The layers visible in the images are due to the three dips applied by dip coating; (b) integrated EDX cross-sectional spectra, before and after 583 days of immersion (reproduced with permission of Elsevier [11]).

2.2 Active protection

2.2.1 Corrosion inhibition by lithium ions

The second requirement for an effective chromium-free coating relies on active anticorrosion protection. Among corrosion inhibitors, it was demonstrated that the incorporation of lithium salts improves corrosion protection of epoxy coatings. As possible mechanisms, Visser et al. have proposed that the release of lithium ions from the epoxy matrix forms in the defective zone a Li/Al layer (hydrotalcite class) by a conversion process [46]. In recent work, lithium carbonate (Li_2CO_3) was for the first time added (500–2000 ppm) into the PMMA-silica system, and the results revealed a dual beneficial effect of lithium on the structure and self-healing ability of the coatings on the AA7075 aluminum alloy [24].

The structural analysis of the coatings showed that the changes of the small-angle X-ray scattering (SAXS) profiles imply significant modifications in the nanostructure of the silica phase for higher lithium loadings (**Figure 5a**). The profiles of Li0 (0 ppm) and Li05 (500 ppm) samples present a correlation peak, indicative of a concentrated set of silica domains with an average spacing of 3–4 nm (**Figure 5b**). However, for further addition of lithium (Li1 and Li2), the correlation peak vanishes due to the formation of a more diluted set of larger silica clusters. For these profiles, the average size of the silica nanoparticles (R_g) can be calculated according to the Guinier-Porod model [47, 48], revealing for the Li1 sample (1000 ppm) a gyration radius of about 1 nm and close to 3 nm for Li2 (2000 ppm).

Thermogravimetric measurements were used to access information on the polymerization efficacy of PMMA and the thermal stability of the material. The results reveal that the samples exhibited a thermal stability up to $\sim 240^\circ\text{C}$ (onset degradation temperature at 5% mass loss, T_s (**Figure 5c**)), while degradation events of the TG derivative curve (**Figure 5d**) showed that the presence of lithium suppresses head-to-head stacking defects (T_1) and unsaturated PMMA chain ends (T_2). These findings indicate a more efficient polymerization with higher Li content, which is an essential feature for an effective diffusion barrier.

The films with thickness between 4 μm and 6 μm present excellent adhesion to AA7075 substrate reaching values up to 28 MPa for coatings with higher Li loading [24]. The improved adhesion for lithium-rich coatings might be related to

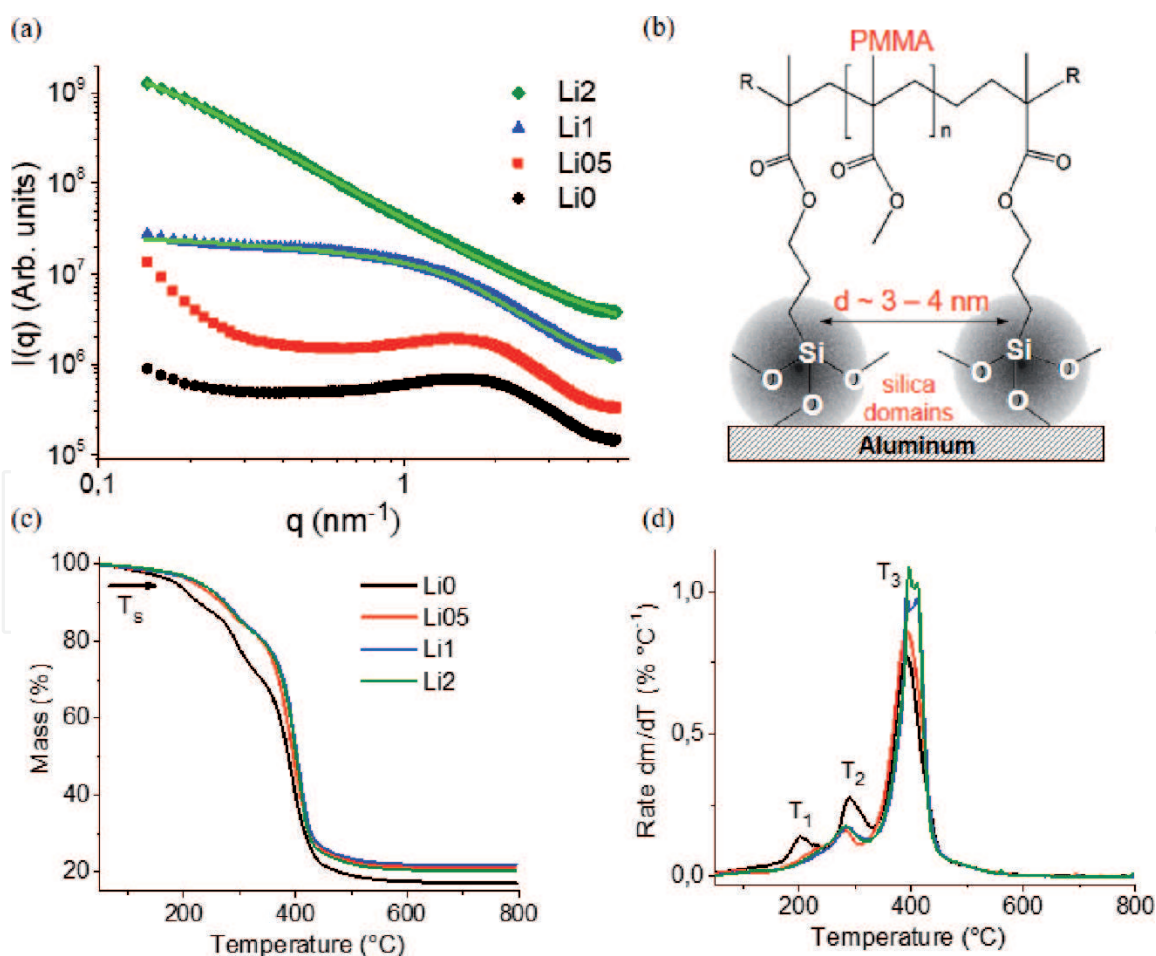


Figure 5. (a) SAXS intensity profiles of the hybrids fitted according to the Guinier-Porod model (green lines); (b) structural representation of Li0 and Li05 PMMA-silica hybrids; (c) thermogravimetric curves and (d) differential thermogravimetric curves of PMMA-silica hybrids prepared with Li_2CO_3 concentrations of 0, 500, 1000, and 2000 ppm (reprinted (adapted) with permission from [24]. Copyright (2020) American Chemical Society).

aluminum enrichment near the coating/substrate interface, suggesting a diffusion of Al from the alloy into the coating during the thermal treatment [24].

Besides the beneficial effects of lithium on the structural properties, Li-modified PMMA-silica hybrids yielded coatings with longer durability under immersion in 3.5% NaCl solution. This is evident from the time dependence of the open circuit potential (E_{OCP}) and the low-frequency impedance modulus ($|Z_{\text{lf}}|$), recorded by EIS during 310 days of immersion (**Figure 6**). For lithium-containing coatings, the time dependence of $|Z_{\text{lf}}|$ (**Figure 6b**) revealed a very interesting effect of coating regeneration, attributed to the chemical activity of the lithium ions. The data show several important features of the lithium activity for different Li loadings: (i) for all samples the time dependence shows a clear correlation between $|Z_{\text{lf}}|$ and E_{OCP} (**Figure 6a**); (ii) after local failure of the coating, an impedance drop occurred, followed by a gradual recovery of about two orders of magnitude within 40 days (Li05), 28 days (Li1), and 20 days (Li2), indicating a faster regeneration process with increasing Li content; and (iii) the higher lithium concentration of Li2 coating delayed the appearance of localized corrosion compared to Li1 and Li05 samples. Furthermore, although the initial value of $|Z_{\text{lf}}|$ was smaller for Li1 and Li2 coatings, after 300 days of immersion, they showed a higher impedance value, an effect that can be related to their improved structural characteristics, as discussed before.

Representatively, the time evolution of the Bode plots obtained by EIS for the Li1 coating is displayed in **Figure 7**, together with the fitted curves (3 h, 99 days, and 126 days) using electrical equivalent circuits (EEC), shown in **Figure 7a**. Initially, Li1 presents an impedance modulus up to six orders of magnitude higher than bare aluminum alloy. As a consequence of the coating permeation by the electrolyte, the formation of conductive percolation paths leads after 99 days to the appearance of localized corrosion spots (pits), causing a decay of the impedance modulus at medium and low frequencies, indicative for failure of the coating and the beginning corrosion process at the coating/metal interface [11]. Nevertheless, after 126 days of immersion, the coating was spontaneously restored, increasing $|Z_{\text{lf}}|$ by two orders of magnitude. Next, the appearance of a second pit caused a new decay after 154 days, and thereafter the impedance modulus has recovered again after 183 days, remaining stable until 311 days of immersion.

The self-healing process of the first recovery event was analyzed by fitting the EIS data using EEC containing an electrolyte resistance in series with two time constants,

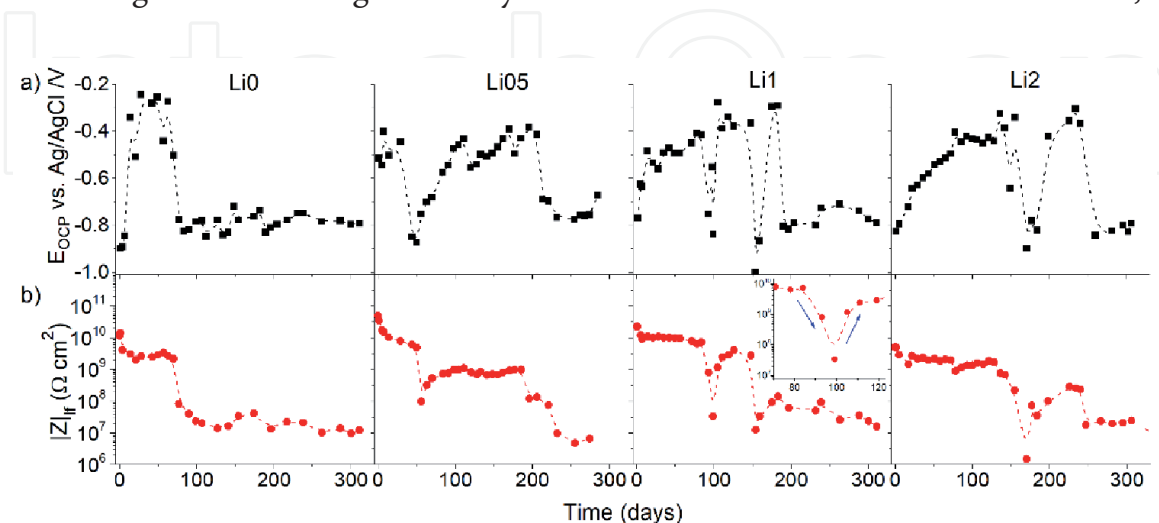


Figure 6. (a) Time evolution of E_{OCP} and (b) $|Z_{\text{lf}}|$ for coatings modified with different amounts of lithium during 310 days of immersion in 3.5% NaCl solution. The inset shows in more detail the first impedance modulus recovery (99 days) for the Li1 sample (reprinted (adapted) with permission from [24]. Copyright (2020) American Chemical Society).

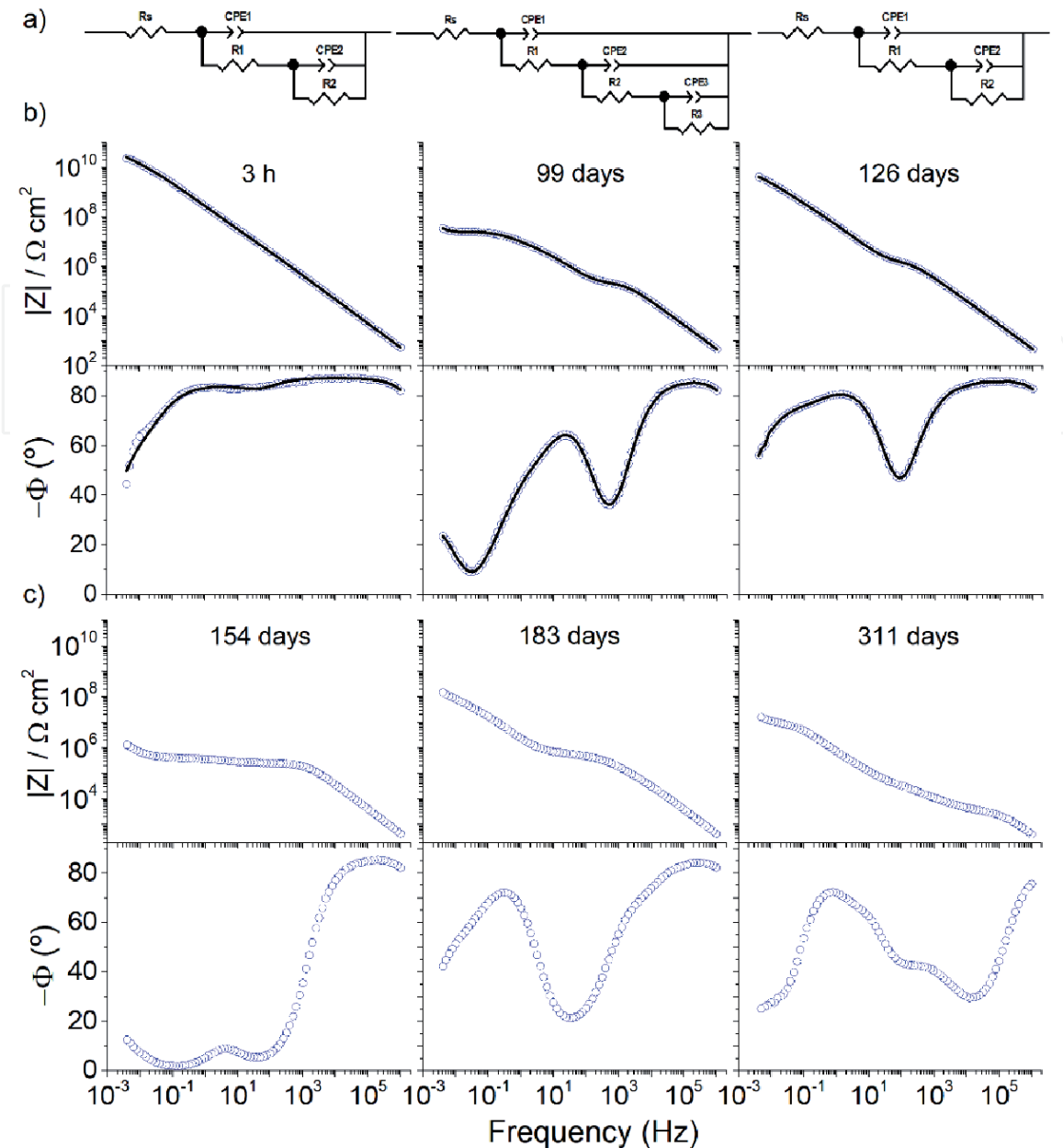


Figure 7.

(a) Electrical equivalent circuits used to fit (black lines) the EIS data of Li1 coating after (b) 3 h, 99 days, and 126 days of immersion in 3.5% NaCl solution and (c) time evolution of the bode plots after 154, 183, and 311 days of immersion (reprinted (adapted) with permission from [24]). Copyright (2020) American Chemical Society).

the first representing the upper water uptake layer and the second the inner intact/restored layer, and by adding a third time constant to simulate the corrosion process at the coating/metal interface (**Figure 7a**). Accordingly, the high-frequency data are generally attributed to phenomena occurring at the coating/electrolyte interface (R_1/CPE_1), the medium frequencies refer to the inner layer of the coating (R_2/CPE_2), and the low frequency is related to charge transfer resistance (R_{ct}) and double-layer capacitance (C_{dl}) at the coating/substrate interface (R_3/CPE_3). The electrochemical parameters, extracted by the fitting procedure, are shown in **Table 2**. After 99 days, a strong decay of R_1 and R_2 can be observed followed by a sharp increase after 126 days, from $0.20 \text{ M}\Omega \text{ cm}^2$ to $1.68 \text{ M}\Omega \text{ cm}^2$ and $0.02 \text{ M}\Omega \text{ cm}^2$ to $9.03 \text{ G}\Omega \text{ cm}^2$, respectively. As expected, an inverse behavior can be observed for the Q values of the CPE parameter, related to the coating capacitance.

To obtain more information on the Li-induced self-healing mechanism, surface analysis by time-of-flight secondary ion mass spectrometry (ToF-SIMS),

Li1	3 h		99 days		126 days	
χ^2	6.4×10^{-3}	—	4.5×10^{-3}	—	5.2×10^{-3}	—
R_s ($\Omega \text{ cm}^2$)	52.8	—	42.4	—	23.0	—
R_1 ($\text{M}\Omega \text{ cm}^2$)	17.1	(12.8)*	0.20	(2.0)	1.68	(2.0)
Q_1 ($\text{n}\Omega^{-1} \text{ cm}^{-2} \text{ s}^n$)	0.46	(2.6)	0.55	(4.1)	0.66	(2.4)
n_1	0.97	(0.2)	0.97	(0.3)	0.95	(0.2)
R_2 ($\text{G}\Omega \text{ cm}^2$)	52.2	(3.8)	0.02	(1.1)	9.03	(3.6)
Q_2 ($\text{n}\Omega^{-1} \text{ cm}^{-2} \text{ s}^n$)	0.21	(5.6)	17.0	(1.8)	3.85	(0.7)
n_2	0.70	(1.6)	0.77	(0.5)	0.88	(0.2)
R_3 ($\text{G}\Omega \text{ cm}^2$)			0.03	(14.6)		
Q_3 ($\text{n}\Omega^{-1} \text{ cm}^{-2} \text{ s}^n$)			2723	(5.1)		
n_3			0.75	(4.9)		

*The values in brackets correspond to the error (%) of each parameter.

Table 2.
 Electrochemical parameters derived by fitting of the EIS data using electrical equivalent circuits of **Figure 7a** for Li1 sample after 3 h, 99 days, and 126 days of immersion in NaCl 3.5%.

X-ray photoelectron spectroscopy (XPS), and SEM were performed. Surface maps recorded by SIMS showed that the pit in the center of the immersion area (**Figure 8b**) contains only two small spots of lithium (red), surrounded by aluminum corrosion products (blue), and PMMA (green) containing a very low Li concentration (**Figure 8a**). In comparison, a higher Li surface concentration was detected outside the immersed area (**Figure 8c**), which indicates a Li^+ leaching process from the coating surface, evidencing its high mobility. Furthermore, the

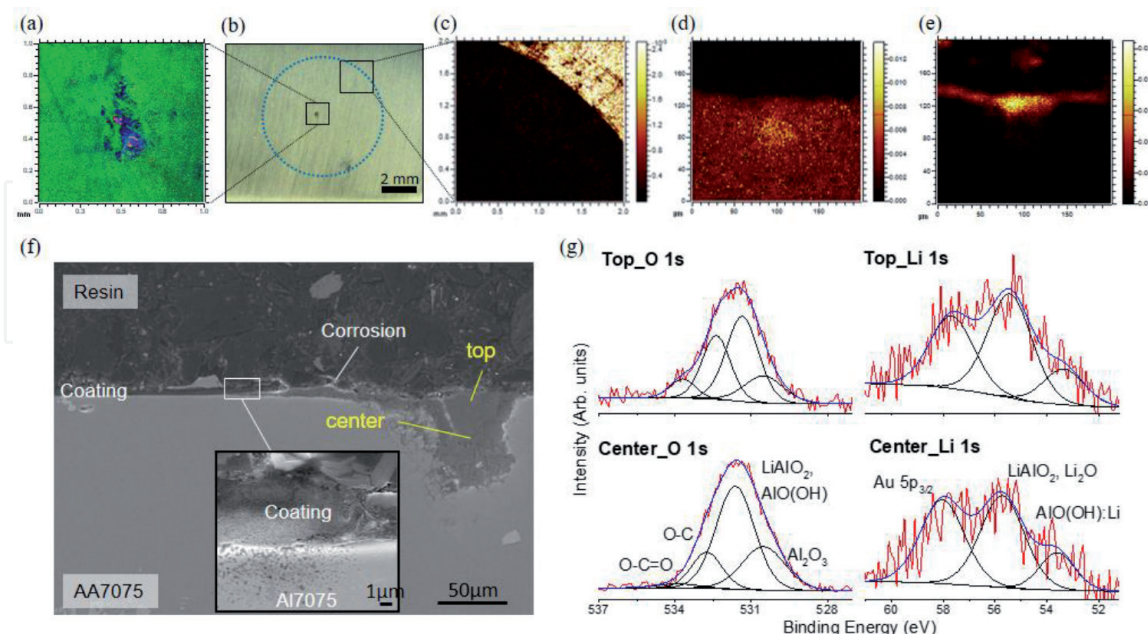


Figure 8.
 (a) ToF-SIMS map of the Li1 coating overlay of Li^+ (red), $\text{C}_2\text{H}_3\text{O}_2^+$ (green), and Al^+ (blue); (b) optical micrograph displaying the immersed area delimited by a blue dashed circle; (c) normalized ToF-SIMS map of Li^+ (yellow) at the edge of the immersed zone; normalized ToF-SIMS maps of (d) AlOH^+ (yellow) and (e) Li^+ (yellow), recorded in top and center zones of **Figure 8f**; (f) SEM cross-sectional view of the pit of the Li1 sample obtained after 310 days of immersion in 3.5% NaCl solution; and (g) fitted XPS O 1s and Li 1s spectra taken at the top and center of the pit. For SEM analysis, sputtered Au was used to improve surface conductivity (reprinted (adapted) with permission from [24]. Copyright (2020) American Chemical Society).

cross-sectional image obtained by SEM (**Figure 8f**) shows a conical shape of the 70- μm -deep pit, surrounded by cathodic debris as a consequence of redox reactions. The cross-sectional SIMS maps of the pit revealed that its center is mainly filled with Al(OH)_x corrosion products (**Figure 8d**) and that the top contains a lithium layer (**Figure 8c**), a clear evidence of the high mobility of lithium ions toward corrosive sites. XPS analysis performed in the top and center zones of the pit (**Figure 8f**) confirmed the SIMS findings, revealing a high Li concentration of 31 at.% and 22 at.%, respectively, and the presence of lithium oxide and lithium-containing aluminum oxide interphases (**Figure 8g**).

The reversible process observed for lithium-containing coatings is related to redox reactions taking place at the coating/substrate interface, as illustrated in **Figure 9**. As soon as water, oxygen, and chloride ions reach the substrate, Cl^- ions form a complex with aluminum producing soluble Al compounds, which cause the pit acidification/propagation. Simultaneously, at the top of the defect, Al(OH)_x begins to precipitate at higher pH (reaction driven by hydroxyl ions, a product of carbonate action), leading to the formation of aluminum oxides. Finally, the curing activity of lithium within the pit is triggered at higher pH by the formation of Li^+ intercalated aluminum oxide phase with a highly passive character [16, 49, 50].

More rigorous tests of lithium self-healing activity were conducted by salt spray tests [24]. SEM images in **Figure 10a** and **b** show that after 7 days of testing, the Li2 sample was almost completely covered by a film, whereas the Li0 sample presents abundant corrosion products in the scratch track. EIS measurements performed after testing revealed for the Li2 coating an increase of the impedance modulus of one decade, while for the Li-free coating, a drop of impedance was observed. A confirmation of Li^+ activity in the corrosion zones was obtained by the overlay of Li^+ (red), AlOH^+ (green) and $\text{C}_2\text{H}_3\text{O}_2^+$ (yellow) SIMS map (**Figure 10c**) showing that lithium ions were preferentially leached from the walls of the scratch to active corrosion zones. The leached Li ions initiated a precipitation reaction of aluminum oxides, resulting in the formation of a protective layer within the scratch track that resulted in a significant reduction of the corrosion rate [46, 51].

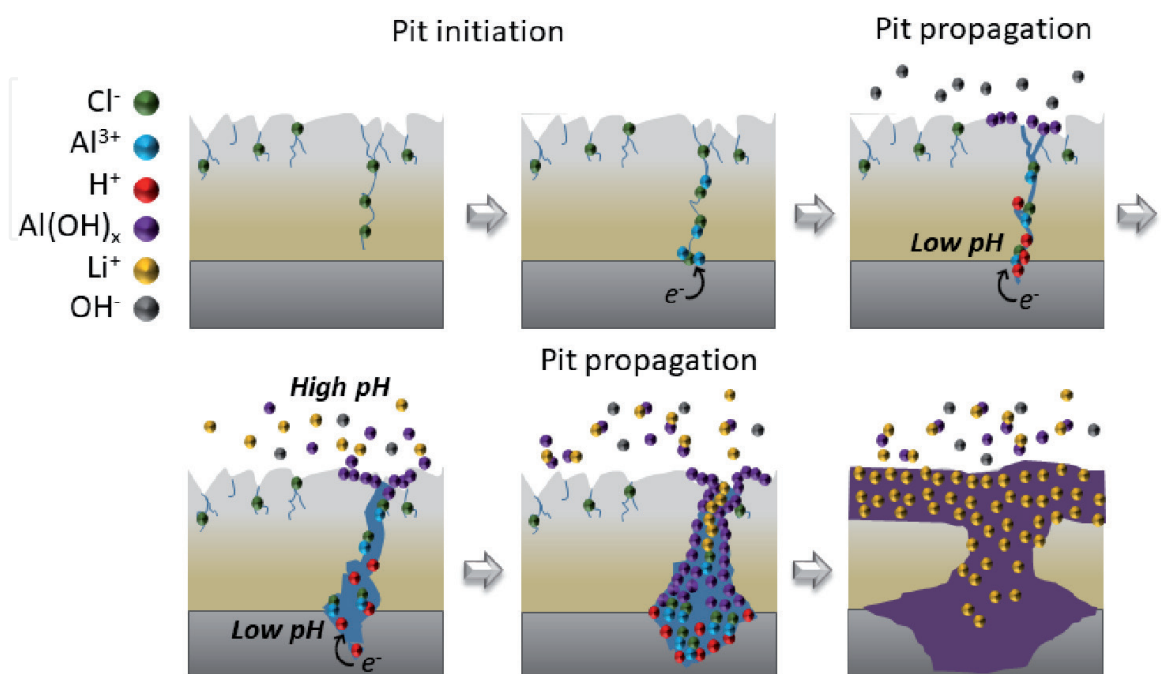


Figure 9. Proposed mechanism for the formation of a lithium-induced protective barrier layer (reprinted (adapted) with permission from [24]. Copyright (2020) American Chemical Society).

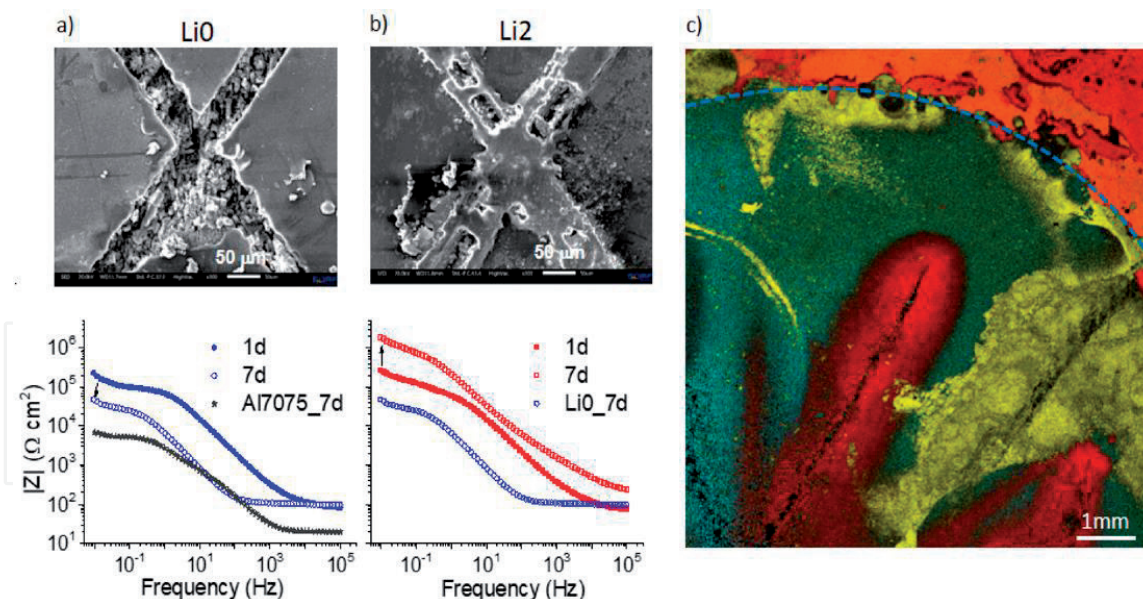


Figure 10. SEM images of the scratched film recorded after 7 days of salt spray test and the corresponding EIS impedance modulus profiles after 1 day and 7 days for (a) LiO and (b) Li₂ coating on Al7075 substrate; (c) ToF-SIMS map of the Li₂ sample showing the overlay map of Li⁺ (red), AlOH⁺ (green), and C₂H₃O₂⁺ (yellow), after 7 days salt spray test (reprinted (adapted) with permission from [24]. Copyright (2020) American Chemical Society).

Structural, surface and electrochemical characterization showed that lithium ions were successfully incorporated into PMMA-silica coatings promoting a beneficial effect on the hybrid structure as well as smart corrosion inhibition. Based on the data of different surface analysis techniques, a self-healing mechanism was proposed that describes a lithium ion-induced formation of a protective layer of redox reaction products that block the corrosion process not only in localized defects (pits) but also in artificially damaged zones, thus extending considerably the service time of the PMMA-silica coating.

2.2.2 Corrosion inhibition by cerium ions

Recently, it was shown that organic-inorganic hybrids based on PMMA-cerium oxide are very promising materials for protective coating due to their excellent corrosion resistance, active self-healing ability, and environmental compatibility [29]. This nanocomposite material was prepared by the radical polymerization of methyl methacrylate and 2-hydroxyethyl methacrylate (HEMA), using benzoyl peroxide as thermal initiator, combined with the sol-gel synthesis of cerium oxide nanoparticles using Ce(NO₃)₃·6H₂O salt and LiOH. The hybrid solutions were used to deposit films on A1020 carbon steel by dip coating, yielding coatings with a thickness of 10 μm. Three coating formulations were evaluated with the following molar proportions, 1Ce:2HEMA:20MMA, 1Ce:2HEMA:25MMA, and 1Ce:2HEMA:30MMA, keeping the BPO/MMA molar ratio equal to 0.05. The HEMA molecule is formed by a methacrylate group that reacts with the organic phase (PMMA) and a hydroxyl terminal group that can be linked to the hydroxyl surface groups of the cerium oxide particles, thus acting as coupling agent and imparting excellent homogeneity and compatibility between the organic and inorganic phases (**Figure 11a**).

Structural characterization performed by XPS, SAXS, and high-resolution transmission electron microscopy (HRTEM) revealed the formation of CeO₂ and Ce₂O₃ nanoparticles with an average size of 2.5 nm and the homogenous distribution of these particles in the PMMA matrix through covalent bonds with the HEMA molecule (**Figure 11b**) [29]. The coatings deposited on carbon steel were transparent

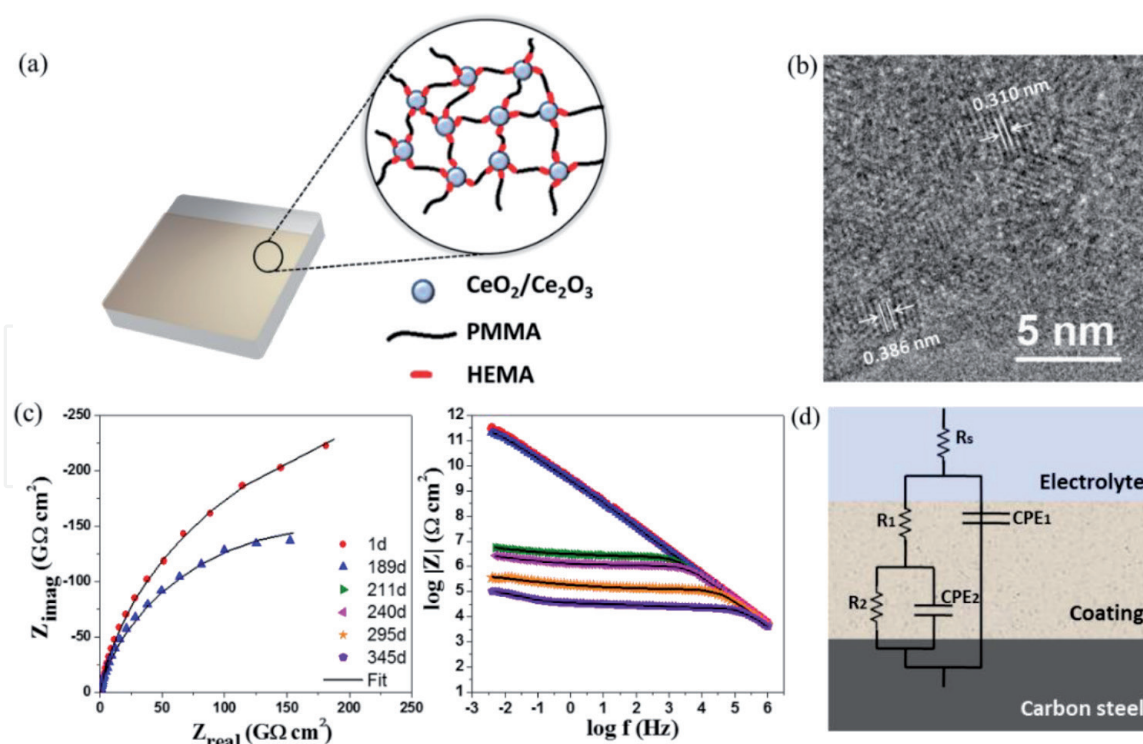


Figure 11.

(a) Schematic representation of the PMMA-cerium oxide coating deposited on carbon steel; (b) HRTEM image of the hybrid; (c) electrochemical impedance spectroscopy plots of the 1Ce:2HEMA:25MMA coating immersed in 3.5% NaCl solution; and (d) electrical equivalent circuit used to fit the EIS data (reproduced with permission from Elsevier [29]).

and free of pores and presented low surface roughness (<1.6 nm), extracted from AFM topography images. In addition, thermogravimetric analysis showed that the PMMA-cerium oxide hybrids have thermal stability up to 220°C and confirmed the nominal inorganic mass fraction for the samples, varying between 22 wt% (1Ce:2HEMA:20MMA) and 10 wt% (1Ce:2HEMA:30MMA).

Careful tuning of the molar ratio between the reagents yielded coatings with notable anticorrosive performance, assessed by electrochemical impedance spectroscopy in aggressive saline environment [29]. The 1Ce:2HEMA:20MMA sample exhibited low corrosion resistance, with impedance modulus at low frequency $|Z_{\text{if}}|$ of $10 \text{ k}\Omega \text{ cm}^2$ after 1 day of immersion in 3.5% NaCl solution, only one order of magnitude higher than the uncoated carbon steel. A small increase of the polymeric content to 1Ce:2HEMA:25MMA, led to a sharp rise of the impedance modulus to $290 \text{ G}\Omega \text{ cm}^2$, which remained almost unchanged after more than 6 months in saline solution (**Figure 11c**). A further increase of the MMA amount to 1Ce:2HEMA:30MMA resulted in an intermediate performance of the coating, with $|Z_{\text{if}}|$ of $95 \text{ G}\Omega \text{ cm}^2$ and durability of 5 months. The corrosion resistance achieved for the 1Ce:2HEMA:25MMA sample is comparable to that of the best anticorrosive coatings reported so far [22, 26, 27, 36, 43, 52–54], however, with the advantage of using nontoxic solvent or precursor. Several interesting results reported for high-performance organic-inorganic coatings with active corrosion protection are summarized in **Table 3**.

The electrical equivalent circuit shown in **Figure 11d** was used to fit the EIS data of the 1Ce:2HEMA:25MMA sample, allowing a deeper insight into the behavior of the electrochemical system. The circuit is composed of a solution resistance (R_s) in series with two time constants (R_1/CPE_1 and R_2/CPE_2) related to coating resistance and capacitance of the near-surface region and that of the inner layer close to the coating/steel interface, respectively. During the immersion period of 189 days,

Coating	Substrate	Thickness (μm)	$ Z_{if} $ ($\text{G}\Omega \text{cm}^2$) 1st failure (days) solution	Ref.
PMMA-MPTS-TEOS-Ce(IV)	A1010 carbon steel	~2	~1, 304, 3.5% NaCl	[26]
PMMA-MPTS-TEOS-Li	AA7075	4–6	~1, 142, 3.5% NaCl	[24]
PMMA-HEMA-CeO ₂	A1010 carbon steel	10	~290, 189, 3.5% NaCl	[29]
PMMA-MPTS-TEOS-Ce	Mild steel	26	~10, 362, 3.5% NaCl	[55]
Epoxy-HT-BZ	Carbon steel	35–45	~10, >60, 0.5 M NaCl	[56]
PVB-p-GAMo	Mild steel	47–53	~1, >21, 3.5% NaCl	[57]
Epoxy-MMT-Ce(III)	Carbon steel	50–70	~0.1, >100, 3.5% NaCl	[58]
Epoxy-PBH-GO	Carbon steel	—	~0.1, 40, 3.5% NaCl	[59]
Epoxy-APS-BS	AA2024	300	~1, >350, 0.5 M NaCl	[60]

PMMA, poly(methyl methacrylate); MPTS, 3-(trimethoxysilyl)propyl methacrylate; TEOS, tetraethoxysilane; Li, lithium; GO, graphene oxide; HT, hydrotalcites; BZ, benzoate; PVB, polyvinyl butyral; p-GAMo, porous organosilica with ion molybdate; MMT, montmorillonite; PBH, polydopamine benzotriazole loaded halloysite nanotubes (HNTs); APS, (3-aminopropyl)trimethoxysilane; BS, bis[3-(triethoxysilyl)propyl]tetrasulfide.

Table 3.
 Reported active hybrid coatings loaded with organic and/or inorganic corrosion inhibitors: composition, substrate, thickness, impedance modulus at low frequency $|Z_{if}|$, time interval until the first failure event occurs, and solution.

the coating resistance of the bulk presented values up to $1 \text{ T}\Omega \text{cm}^2$ and coating capacitance of less than 0.1 nF cm^{-2} , characteristics of an extremely efficient anti-corrosion barrier arising from the dense and highly insulating cross-linked PMMA-cerium oxide structure [29].

Moreover, a detailed analysis of scratched and immersed coatings performed by EIS, XPS, and SEM (Figure 12) evidenced that Ce ions act as self-healing agents, by formation of insoluble cerium oxide and hydroxide species by reactions between leached cerium ions and hydroxyl groups in the scratch track, inhibiting the progression of the corrosion process and consequently enhancing the coating lifetime [29].

In summary, PMMA-cerium oxide coatings deposited on carbon steel combine high corrosion resistance, durability, self-healing property, low-cost, small-thickness, and eco-friendliness, thus representing a very promising alternative to conventional anticorrosive coatings for the protection of steel components.

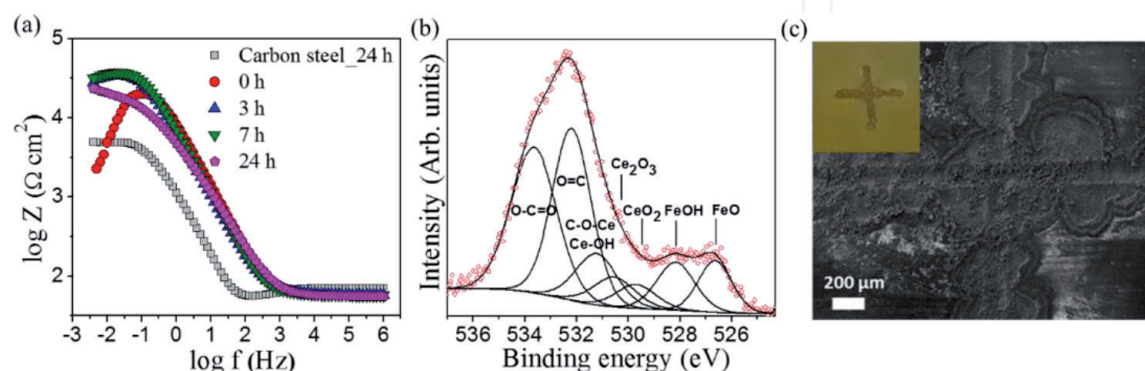


Figure 12.
 (a) EIS plot of the scratched PMMA-cerium oxide coating immersed in 3.5% NaCl solution; (b) XPS O 1s spectra and (c) SEM image after immersion in 3.5% NaCl solution for 24 h (reproduced with permission from Elsevier [29]).

3. Conclusions

Advances in the search for effective substituents of chromates claim long-term protection through a dense barrier coating associated with an active response in case of damage. In this chapter, we have shown that acrylic nanocomposites efficiently prevent corrosion for 583 days by applying a thin (10 μm), adherent (up to 26 MPa), and transparent (80–90% transmission) layer of PMMA-silica on carbon steel. Furthermore, it was demonstrated that by incorporation of corrosion inhibitors, such as lithium ions and cerium oxide nanoparticles, a self-healing ability of hybrid coatings can be achieved, based on different mechanisms: lithium ions induce the formation of a passive layer in the corroded zone composed of Li^+ intercalated aluminum oxide phases, whereas cerium nanoparticles liberate cerium ions that react with water to form insoluble oxides and hydroxides in the affected zone, thus blocking the progress of the corrosion process of the AA7075 alloy and carbon steel, respectively. The efficient passive and active protection of metallic surfaces makes acrylic hybrid coatings potential candidates for a chromate-free future.

Acknowledgements

The authors would like to acknowledge the financial support of funding agencies, namely, Conselho Nacional de Desenvolvimento Científico e Tecnológico (CNPq) [grants 424133/2016-4, 307905/2018-7, 421081/2016-3], Coordenação de Aperfeiçoamento de Pessoal de Nível Superior (CAPES) [grants 465593/2014-3 and 88887.136401/2017-2100, Finance Code 001], and Fundação de Amparo à Pesquisa do Estado de São Paulo (FAPESP) [grants 2015/11907-2, 2015/09342-7, 2014/12182-9]. We also thank the National Laboratory of Synchrotron Light Source (LNLS) for SAXS beamline access and LNNano for the HRTEM images, the Hercules program under grant agreement ZW13_07 for ToF-SIMS measurements, and the Electrochemical and the Surface Engineering Group (SURF, Brussels/Belgium) for the SEM and EDX analysis.

Conflict of interest

The authors declare no conflict of interest.

IntechOpen

IntechOpen

Author details

Andressa Trentin, Samarah V. Harb, Thiago A.C. de Souza, Mayara C. Uvida
and Peter Hammer*
Institute of Chemistry, São Paulo State University (UNESP), Araraquara, SP, Brazil

*Address all correspondence to: peter.hammer@unesp.br

IntechOpen

© 2020 The Author(s). Licensee IntechOpen. This chapter is distributed under the terms of the Creative Commons Attribution License (<http://creativecommons.org/licenses/by/3.0>), which permits unrestricted use, distribution, and reproduction in any medium, provided the original work is properly cited. 

References

- [1] Callister WD Jr, Rethwisch DG. *Materials Science and Engineering: And Introduction*. 9th ed. Hoboken: Wiley; 2014
- [2] Lumley RN. Introduction: Aluminium, the strategic material. In: Lumley RN, editor. *Fundamentals of Aluminium Metallurgy. Recent Advances*. Duxford: Woodhead Publishing; 2018. pp. 17-30
- [3] Harb SV, Trentin A, Torrico RFO, et al. Organic-inorganic hybrid coatings for corrosion protection of metallic surfaces. In: Giudice C, Canosa G, editors. *New Technologies in Protective Coatings*. Rijeka: IntechOpen; 2017. pp. 19-51
- [4] Fischer HR, García SJ. Active protective coatings: Sense and heal concepts for organic coatings. In: Zheludkevich ML, Buchheit RG, Hughes AE, et al., editors. *Active Protective Coatings: New-Generation Coatings for Metals*. Dordrecht: Springer Science+Business Media B.V; 2016. pp. 139-156
- [5] Hughes AE, Mol JMC, Zheludkevich ML, et al. Introduction. In: Hughes AE, Mol JMC, Zheludkevich ML, et al., editors. *Active Protective Coatings: New-Generation Coatings for Metals*. Dordrecht: Springer Science+Business Media B.V; 2016. pp. 1-13
- [6] Fedrizzi L, Andreatta F. Corrosion inhibitors. In: Hughes RAE, Mol JMC, Zheludkevich ML, editors. *Active Protective Coatings: New-Generation Coatings for Metals*. Dordrecht: Springer Science+Business Media B.V; 2016. pp. 59-84
- [7] IARC Working Group. Chromium (VI) compounds. In: Galichet L, editor. *Arsenic, Metals, Fibres and Dusts. A Review of Human Carcinogens*. International Agency for Research on Cancer; 2012. pp. 147-164
- [8] Echeverría M, Abreu CM, Lau K, et al. Viability of epoxy-siloxane hybrid coatings for preventing steel corrosion. *Progress in Organic Coatings*. 2016;**92**:29-43
- [9] Del Angel-López D, Domínguez-Crespo MA, Torres-Huerta AM, et al. Analysis of degradation process during the incorporation of ZrO₂:SiO₂ ceramic nanostructures into polyurethane coatings for the corrosion protection of carbon steel. *Journal of Materials Science*. 2013;**48**:1067-1084
- [10] Harb SV, Trentin A, Uvida MC, et al. A comparative study on PMMA-TiO₂ and PMMA-ZrO₂ protective coatings. *Progress in Organic Coatings*. 2019;**140**:105477
- [11] Trentin A, Gasparini AL, Faria FA, et al. Barrier properties of high performance PMMA-silica anticorrosion coatings. *Progress in Organic Coatings*. 2020;**138**:105398
- [12] Dos Santos FC, Harb SV, Menu MJ, et al. On the structure of high performance anticorrosive PMMA-siloxane-silica hybrid coatings. *RSC Advances*. 2015;**5**:106754-106763
- [13] Gandhi JS, Singh S, Van Ooij WJ, et al. Evidence for formation of metallo-siloxane bonds by comparison of dip-coated and electrodeposited silane films. *Journal of Adhesion Science and Technology*. 2006;**20**:1741-1768
- [14] Torrico RFAO, Harb SV, Trentin A, et al. Structure and properties of epoxy-siloxane-silica nanocomposite coatings for corrosion protection. *Journal of Colloid and Interface Science*. 2018;**513**:617-628
- [15] Sorensen PA, Kiil S, Dam-Johansen K, et al. Anticorrosive

coatings: A review. *Journal of Coatings Technology and Research*. 2009;**6**:135-176

[16] Grundmeier G, Schmidt W, Stratmann M. Corrosion protection by organic coatings: Electrochemical mechanism and novel methods of investigation. *Electrochimica Acta*. 2000;**45**:2512-2533

[17] Sanchez C, Belleville P, Popall M, et al. Applications of advanced hybrid organic-inorganic nanomaterials: From laboratory to market. *Chemical Society Reviews*. 2011;**40**:696-753

[18] Alessi S, Toscano A, Pitarresi G, et al. Water diffusion and swelling stresses in ionizing radiation cured epoxy matrices. *Polymer Degradation and Stability*. 2017;**144**:137-145

[19] Blaiszik BJ, Kramer SLB, Olugebefola SC, et al. Self-healing polymers and composites second Sandia fracture challenge view project shock wave energy dissipation by mechanochemically-active materials view project self-healing polymers and composites. *Annual Review of Materials Research*. 2010;**40**:179-211

[20] Qiu S, Chen C, Zheng W, et al. Long-term corrosion protection of mild steel by epoxy coating containing self-doped polyaniline nanofiber. *Synthetic Metals*. 2017;**229**:39-46

[21] Maya-Visuet E, Gao T, Soucek M, et al. The effect of TiO₂ as a pigment in a polyurethane/polysiloxane hybrid coating/aluminum interface based on damage evolution. *Progress in Organic Coatings*. 2015;**83**:36-46

[22] Ammar S, Ramesh K, Vengadaesvaran B, et al. Amelioration of anticorrosion and hydrophobic properties of epoxy/PDMS composite coatings containing nano ZnO particles. *Progress in Organic Coatings*. 2016;**92**:54-65

[23] Visser P, Marcoen K, Trindade GF, et al. The chemical throwing power of lithium-based inhibitors from organic coatings on AA2024-T3. *Corrosion Science*. 2019;**150**:194-206

[24] Trentin A, Harb SV, Uvida MC, et al. Dual role of lithium on the structure and self-healing ability of PMMA-silica coatings on AA7075 alloy. *ACS Applied Materials & Interfaces*. 2019;**11**:40629-40641

[25] Lv X, Li X, Li N, et al. ZrO₂ nanoparticle encapsulation of graphene microsheets for enhancing anticorrosion performance of epoxy coatings. *Surf and Coatings Technology*. 2019;**358**:443-451

[26] Harb SV, Dos Santos FC, Caetano BL, et al. Structural properties of cerium doped siloxane-PMMA hybrid coatings with high anticorrosive performance. *RSC Advances*. 2015;**5**:15414-15424

[27] Calado LM, Taryba MG, Carmezim MJ, et al. Self-healing ceria-modified coating for corrosion protection of AZ31 magnesium alloy. *Corrosion Science*. 2018;**142**:12-21

[28] Schem M, Schmidt T, Gerwann J, et al. CeO₂-filled sol-gel coatings for corrosion protection of AA2024-T3 aluminium alloy. *Corrosion Science*. 2009;**51**:2304-2315

[29] Harb SV, Trentin A, de Souza TAC, et al. Effective corrosion protection by eco-friendly self-healing PMMA-cerium oxide coatings. *Chemical Engineering Journal*. 2019;**383**:123219

[30] Chen C, Qiu S, Cui M, et al. Achieving high performance corrosion and wear resistant epoxy coatings via incorporation of noncovalent functionalized graphene. *Carbon*. 2017;**114**:356-366

[31] Xia Z, Liu G, Dong Y, et al. Anticorrosive epoxy coatings based on

- polydopamine modified molybdenum disulfide. *Progress in Organic Coatings*. 2019;**133**:154-160
- [32] Khodabakhshi J, Mahdavi H, Najafi F. Investigation of viscoelastic and active corrosion protection properties of inhibitor modified silica nanoparticles/epoxy nanocomposite coatings on carbon steel. *Corrosion Science*. 2019;**147**:128-140
- [33] Nardeli JV, Fugivara CS, Taryba M, et al. Tannin: A natural corrosion inhibitor for aluminum alloys. *Progress in Organic Coatings*. 2019;**135**:368-381
- [34] Brinker CJ, Scherer GW. Sol → gel → glass: I. Gelation and gel structure. *Journal of Non-Crystalline Solids*. 1985;**70**:301-322
- [35] Lou C, Zhang R, Lu X, et al. Facile fabrication of epoxy/polybenzoxazine based superhydrophobic coating with enhanced corrosion resistance and high thermal stability. *Colloids Surfaces A*. 2019;**562**:8-15
- [36] Lamaka SV, Xue HB, Meis NNAH, et al. Fault-tolerant hybrid epoxy-silane coating for corrosion protection of magnesium alloy AZ31. *Progress in Organic Coatings*. 2015;**80**:98-105
- [37] He P, Wang J, Lu F, et al. Synergistic effect of polyaniline grafted basalt plates for enhanced corrosion protective performance of epoxy coatings. *Progress in Organic Coatings*. 2017;**110**:1-9
- [38] Díaz I, Chico B, De La Fuente D, et al. Corrosion resistance of new epoxy-siloxane hybrid coatings. A laboratory study. *Progress in Organic Coatings*. 2010;**69**:278-286
- [39] Ashhari S, Sarabi AA, Kasiriha SM, et al. Aliphatic polyurethane-montmorillonite nanocomposite coatings: Preparation, characterization, and anticorrosive properties. *Journal of Applied Polymer Science*. 2011;**119**:523-529
- [40] Lu F, Song B, Wang J. Preparation and characterization of acrylic polyurethane/polyaniline nanocomposite coatings. *International Journal of Electrochemical Science*. 2017;**12**:2679-2691
- [41] Hammer P, Dos Santos FC, Cerrutti BM, et al. Highly corrosion resistant siloxane-polymethyl methacrylate hybrid coatings. *Journal of Sol-Gel Science and Technology*. 2012;**63**:266-274
- [42] Harb SV, Pulcinelli SH, Santilli CV, et al. A comparative study on graphene oxide and carbon nanotube reinforcement of PMMA-siloxane-silica anticorrosive coatings. *ACS Applied Materials & Interfaces*. 2016;**8**:16339-16350
- [43] Ammar S, Ramesh K, Vengadaesvaran B, et al. A novel coating material that uses nano-sized SiO₂ particles to intensify hydrophobicity and corrosion protection properties. *Electrochimica Acta*. 2016;**220**:417-426
- [44] Alrashed MM, Jana S, Soucek MD. Corrosion performance of polyurethane hybrid coatings with encapsulated inhibitor. *Progress in Organic Coatings*. 2019;**130**:235-243
- [45] He Z, Li X, Soucek MD, et al. Inhibition of acid undercutting of inorganic/organic hybrid polyurethane coatings. *Progress in Organic Coatings*. 2019;**134**:169-176
- [46] Visser P, Lutz A, Mol JMC, et al. Study of the formation of a protective layer in a defect from lithium-leaching organic coatings. *Progress in Organic Coatings*. 2016;**99**:80-90
- [47] Guinier G, Fournet C, Walker CB, et al. *Small Angle Scattering of Xrays*. New York: Freeman; 1955

- [48] Hammouda B. A new Guinier-Porod model. *Journal of Applied Crystallography*. 2010;**43**:716-719
- [49] Foley RT. Localized corrosion of aluminum alloys—A review. *Corrosion*. 1986;**42**:277-288
- [50] Reboul MC, Warner T, Mayet H, et al. A ten-step mechanism for the pitting corrosion of aluminium. *Materials Science Forum*. 1996;**217-222**:1553-1558
- [51] Isupov VP. Intercalation compounds of aluminum hydroxide. *Journal of Structural Chemistry*. 1999;**40**:672-682
- [52] Thai TT, Druart M-E, Paint Y, et al. Influence of the sol-gel mesoporosity on the corrosion protection given by an epoxy primer applied on aluminum alloy 2024-T3. *Progress in Organic Coatings*. 2018;**121**:53-63
- [53] Wang N, Gao H, Zhang J, et al. Effect of graphene oxide/ZSM-5 hybrid on corrosion resistance of waterborne epoxy coating. *Coatings*. 2018;**8**:1-14
- [54] Ramezanzadeh B, Bahlakeh G, Ramezanzadeh M. Polyaniline-cerium oxide (PAni-CeO₂) coated graphene oxide for enhancement of epoxy coating corrosion protection performance on mild steel. *Corrosion Science*. 2018;**137**:111-126
- [55] Mosa J, Rosero-Navarro NC, Aparicio M. Active corrosion inhibition of mild steel by environmentally-friendly Ce-doped organic-inorganic sol-gel coatings. *RSC Advances*. 2016;**6**:39577-39586
- [56] Nguyen Thuy D, To Thi Xuan H, Nicolay A, et al. Corrosion protection of carbon steel by solvent free epoxy coating containing hydrotalcites intercalated with different organic corrosion inhibitors. *Progress in Organic Coatings*. 2016;**101**:331-341
- [57] Lin Y, Chen R, Zhang Y, et al. Application of porous organosilica intercalated graphene oxide as the container of molybdate inhibitors for anticorrosive coatings. *Materials and Design*. 2020;**186**:108304
- [58] Danaee I, Darmiani E, Rashed GR, et al. Self-healing and anticorrosive properties of Ce(III)/Ce(IV) in nanoclay-epoxy coatings. *Iranian Polymer Journal*. 2014;**23**:891-898
- [59] Chen C, Xiao G, He Y, et al. Bio-inspired superior barrier self-healing coating: Self-assembly of graphene oxide and polydopamine-coated halloysite nanotubes for enhancing corrosion resistance of waterborne epoxy coating. *Progress in Organic Coatings*. 2019;**139**:105402
- [60] Abdolah Zadeh M, Van Der Zwaag S, Garcia SJ. Adhesion and long-term barrier restoration of intrinsic self-healing hybrid sol-gel coatings. *ACS Applied Materials & Interfaces*. 2016;**8**:4126-4136